ACS APPLIED NANO MATERIALS

www.acsanm.org Article

Metal Sulfide Thin Films with Tunable Nanoporosity for Photocatalytic Applications

Efthymia Vakalopoulou, Thomas Rath,* Marianne Kräuter, Ana Torvisco, Roland C. Fischer, Birgit Kunert, Roland Resel, Hartmuth Schröttner, Anna Maria Coclite, Heinz Amenitsch,* and Gregor Trimmel

Cite This: *ACS Appl. Nano Mater.* 2022, 5, 1508−1520 Read Online

ACCESS | Metrics & More | Article Recommendations | Supporting Information

ABSTRACT: Metal xanthates are widely used as single-source precursors for the formation of metal sulfide thin films. In this study, we explore the length of the alkyl ligand as an efficient tool to control the formation and the nanoporosity of zinc sulfide thin films. The presented approach allows us to prepare highly porous thin metal sulfide films with potential applications in photocatalysis, whereby the nanoporosity is significantly enhanced with an increasing number of carbons in the alkyl chain of the metal xanthate precursors. To gain knowledge about the mechanisms leading to the changes in the nanoporosity, the thermal conversion process toward the porous films is studied in detail by time-resolved simultaneous grazing incidence small- and wide-angle X-ray scattering measurements using synchrotron radiation and thermogravimetric analysis. Thereby, we found that the structural changes during the early stages of the conversion process, which are distinctly influenced by the decomposition temperature of the metal xanthates, different growth regimes of the nanocrystals, and a mesophase formation, governed by the properties of the decomposition products of the metal xanthates, are mainly responsible for the changes of the structural properties and the nanoporosity of the final ZnS films.

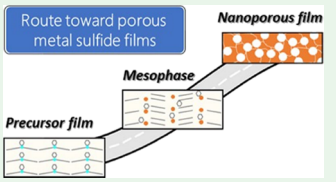

KEYWORDS: *zinc sulfide, metal xanthate, time-resolved GISAXS, conversion mechanism, single-source precursor, template-free*

INTRODUCTION

Porous materials are essential elements in many highly relevant technologies such as catalysis, sensing, separation processes, and energy storage.[1−3] Compared to porous bulk materials, the synthesis of porous thin films brings additional challenges in terms of processing, film formation, and characterization. Examples regarding the formation of porous thin films in the literature include mainly metal oxides such as TiO_2,[4,5] SiO_2,[6] and ZnO,[7−10] while lately metal−organic framework (MOF) thin layers also have been attracting increased attention.[11−14] The standard method used for the preparation of the abovementioned porous metal oxide thin films is the soft-templating technique. This technique utilizes surfactants, which have the ability to (i) form either micelles, which can self-assemble within the thin film, such as CTAB[15] or Pluronic F-127,[16] or (ii) build ordered monolayers on the substrates, such as polystyrene microspheres,[17,18] or (iii) form complexes with the precursor materials, such as the copolymer PEG.[19]

Regarding porous metal sulfide thin films, there are only very few studies reported in the literature,[20−22] even though the benefits of porosity in combination with the properties of metal sulfides can be a powerful tool for improving the existing applications of this class of materials. The main method toward porous metal sulfides employs templates, whereby, in particular, soft-templating or hard-templating, also known as nanocasting, routes are employed. The soft-templating route uses structure directing agents, such as lyotropic liquid crystalline templates, which provide mesostructured metal sulfide films.[23] On the other hand, the nanocasting method has two separate steps. Herein, first the porous hard template, such as mesoporous silica, is formed via soft-templating and subsequently the precursors are infiltrated. In the second step, the template is removed typically with the use of HF in order to provide a mesoporous metal sulfide thin layer.[24,25] However, there also exist studies on less common template-free methods toward porous metal sulfides, targeting to overcome problems derived from the template-assisted methods, such as the use of harmful chemicals (e.g., HF),[24] or stability issues during the removal of the structure directing agents.[23] In one example, copper zinc tin sulfide (CZTS) thin films were obtained using a simple template-free solvothermal route;[20] in another, nickel and cobalt sulfide thin films were prepared via a one-step template-free flame synthesis method.[26]

In this study, we present the formation of nanoporous ZnS films with tunable porosity via a one-step process with the use of zinc xanthates. Metal xanthates, also known as metal dithiocarbonates, belong to the group of single-source

Received: December 6, 2021
Accepted: December 20, 2021
Published: January 4, 2022

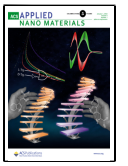

precursors, which are used for the formation of metal sulfides.[27,28] The characteristic feature of these compounds is the metal−sulfur bond. At room temperature, the metal xanthates show high stability, but upon thermal treatment, they decompose and are converted to metal sulfides. The conversion can take place in solution and in solid-state reactions. Commonly, their thermal decomposition proceeds via a mechanism known as Chugaev elimination, which leads to the formation of COS (carbonyl sulfide) and the corresponding alkene.[29] Very recently, we found that a second mechanism, in which the xanthate is protonated and leads to the formation of CS_2 and the corresponding alcohol, occurs simultaneously with the Chugaev elimination.[30] Even though thermal decomposition is the most conventional method, metal xanthates can also be decomposed chemically[31,32] or photochemically,[33] with primary amines or UV irradiation, respectively. There are many studies where metal xanthates are used for the formation of nanocrystalline metal sulfides, either as powders[30,34,35] or thin films on substrates.[36−39] In these approaches, metal xanthates are initially dissolved in an appropriate solvent forming a clear solution and are subsequently deposited on substrates via several possible methods such as spin-coating,[40,41] doctor blading,[42] or chemical vapor deposition.[43−45] The next step is their decomposition and conversion to metal sulfides. The prepared metal sulfides can be further used in applications, such as solar cells,[46,47] curing agents for epoxy resins,[48] and supercapacitors or catalysts for water splitting.[49,50]

Herein, the novel template-free formation of nanoporous metal sulfide films via a one-step solution-based route is demonstrated using zinc sulfide (ZnS) as a model compound and we foresee facile applicability of this route to further binary or ternary metal sulfides, which can be applied as nanoporous films in a wide range of photocatalysis or energy conversion or storage applications.[51−53] A particular focus of this study is set on disclosing the processes behind this one-step formation of the porous metal sulfide films and the influence of the alkyl ligand length on the formation process and the porosity of the ZnS films. This is thoroughly investigated at the nanometer scale, among further techniques, in particular, via X-ray reflectivity, ellipsometric porosimetry, and time-resolved grazing incidence small- and wide-angle X-ray scattering measurements using synchrotron radiation.

RESULTS AND DISCUSSION

Zinc xanthates with alkyl ligands comprising 2, 5, 6, and 12 carbon atoms have been synthesized as outlined in Figure 1a and in the Experimental Section according to previous studies.[30,54,55] Due to the low solubility of these compounds in common organic solvents, such as chloroform and toluene,[56] they have been modified with pyridine ligands, which leads to a significant increase of their solubility. In the following text, the zinc xanthate complexes and the ZnS films prepared with these precursors will be referred to as C-x (x = 2, 5, 6, and 12, depending on the number of carbon atoms in the linear aliphatic alkyl chain).

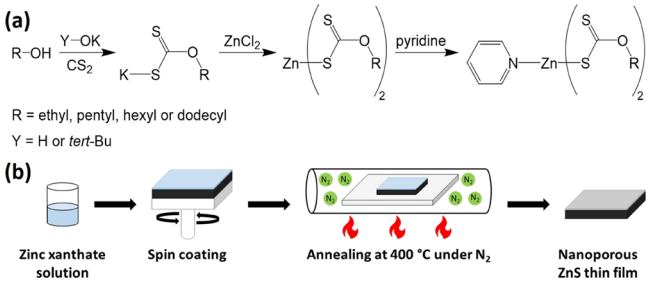

Figure 1. (a) Synthesis of zinc xanthate precursors with different alkyl chains. (b) Schematic presentation of the nanoporous ZnS thin-film formation.

The zinc xanthate complexes were analyzed by ^{1}H nuclear magnetic resonance (NMR), ^{13}C NMR, and Fourier transform infrared (FTIR) spectroscopies. The signals in the ^{13}C NMR spectra show the typical chemical shifts, and the peak at approximately 230 ppm corresponds to the dithiocarbonate group (S_2COR). The quantitative analysis of the ^{1}H NMR spectra reveals that there is one pyridine ligand bound to the zinc atoms (Figure S2). Additionally, the FTIR spectra of the compounds are in accordance with the suggested structure, demonstrating the characteristic vibrational bands at approximately 1200, 1140, and 1040 cm^{-1}, which correspond to symmetric and asymmetric stretching vibrations of COC and S(CO) and asymmetric stretching vibrations of SCS, respectively. Moreover, the three bands at 1608, 1483, and 1446 cm^{-1} are assigned to plane vibrations of C=C and C=N of the pyridine ligand.[57]

Additionally, it was possible to obtain single crystals of C-6 and C-12 and thus the single-crystal X-ray diffraction analysis was performed, which revealed the crystal structures shown in Figure S3. The sample C-5 gave no crystals with quality for single-crystal X-ray diffraction. The crystal structure of the $Zn(S_2COEt)_2(C_5H_5N)$ complex (C-2) was already studied by Raston et al. in 1976.[58] These compounds show many similarities regarding the ligand coordination and bond lengths and angles. They are square pyramidally coordinated with the nitrogen atom of the pyridine ligand and the two sulfur atoms of the two symmetrical xanthate ligands. The same coordination was found in our previous study on zinc di(*O*-2,2-dimethylpentan-3-yl)dithiocarbonate bearing a pyridine coligand (ZnHepPyr).[30] Moreover, the analysis of the data reveals a monodentate coordination of the nitrogen on the zinc atom with a bond length of 2.0229(10) and 1.973(6) Å for C-6 and C-12, respectively. The xanthate ligands are bidentally coordinated on the metal atom with both sulfur atoms. The complexes exhibit one strong and one weak Zn−S bond on each xanthate ligand. The same result is also presented in the literature for $Zn(S_2COEt)_2(C_5H_5N)$.[58] Geometric parameters are provided in Table S1 for C-6 and Table S2 for C-12, respectively.

For the preparation of the nanoporous ZnS films, which is schematically outlined in Figure 1b, the zinc xanthate complexes were dissolved in chloroform. These precursor solutions were deposited via spin-coating onto silicon or glass substrates followed by thermal annealing at 400 °C under a continuous N_2 flow, resulting in clear and semitransparent films. To obtain similar film thicknesses ranging between 83 and 90 nm, the concentration of the precursor solution had to be reduced from 0.26 for C-2 to 0.15 mmol/L for C-12 (see Table S4). This gives the first hint toward increasing porosities obtained in the films prepared from metal xanthates with longer alkyl side chains. To exclude the possibility of incomplete decomposition of the larger precursor compounds at 400 °C, FTIR measurements before and after decomposition were performed (Figures 2 and S6). The spectra of films of the zinc xanthate complexes before decomposition are

https://doi.org/10.1021/acsanm.1c04206
ACS Appl. Nano Mater. 2022, 5, 1508−1520

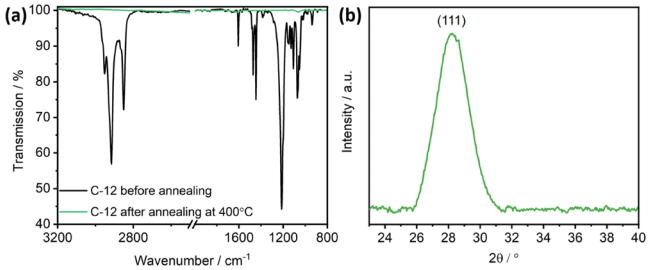

Figure 2. (a) FTIR spectra of C-12 films on silicon wafers before (black spectrum) and after annealing at 400 °C (green spectrum). (b) GIWAXS pattern of the C-12 film showing the ZnS (111) reflection after annealing at 400 °C.

in agreement with the spectra of the respective powdered materials (Figure S1), exhibiting all the typical vibrations of the metal xanthate complexes discussed earlier. On the contrary, after decomposition, all the IR bands have completely disappeared, which indicates the elimination of all the organic residues from the films. Thus, the most obvious explanation for the observed similar thicknesses is a difference in the porosity of the films, which is investigated in more detail in the further course of this study. The formation of ZnS films after the thermal conversion is confirmed by the distinct diffraction peak at 28.2° 2θ in the grazing incidence wide-angle X-ray scattering (GIWAXS) patterns (shown for the C-12 sample in Figure 2b), which is characteristic for the (111) reflection of cubic ZnS. Moreover, X-ray diffraction (XRD) patterns of powders prepared by the thermal conversion of the powdered zinc xanthate precursors C-2, C-5, C-6, and C-12 at 400 °C reveal the formation of ZnS for the four investigated zinc xanthates (Figure S4).

To gain more information regarding the compactness of the ZnS films, X-ray reflectivity (XRR) measurements were performed, which allow the extraction of the electron densities of ZnS films. The XRR intensity curves of the four ZnS films prepared from the metal xanthate precursors with increasing alkyl chain lengths are shown in Figure 3a. The XRR signal is strongly influenced by the thin film's electron density, ρ_{el}. The relation is given as:

$$\rho_{el} = \frac{\pi}{\lambda^2 r_e}\theta_c^2 \quad (1)$$

where λ is the X-ray wavelength, r_e is the electron radius (2.813×10^{-6} nm), and θ_c is the critical angle (in radian), where the total reflection of the X-rays occurs. The critical angle, θ_c, is determined by the point of the sharp decay in the XRR intensity.[24,59] The reflectivity curves of the ZnS films with the different xanthate complexes (Figure 3a) display pronounced changes in the critical angles and as a result also different electron densities. More specifically, the electron density decreases with the increasing alkyl ligand length. Table S6 lists the electron densities of the four measured ZnS films and a reference value for bulk ZnS calculated according to eq S1 in the Supporting Information. The decreasing electron densities with the increasing length of the alkyl ligand indicate a decrease of the compactness of the films from C-2 to C-5/C-6 and finally to C-12. The latter suggests the potential presence of increasing empty space (pores) within the films prepared from the precursors with longer alkyl chains. While the electron density of the C-2 sample is significantly higher than that of the C12 sample (8.51 and 6.15 $\times$ 10^{23}/cm^{-3}, respectively), the electron densities of the C-5 and C-6 samples lie between these two values and are very similar, which is expected due to only a small difference in the alkyl chain length (see Table S6). The fact that the electron density of the C-5 sample is even slightly lower is most probably due to the few macroscopic holes observed in the scanning electron microscopy (SEM) images, which can slightly influence the XRR measurements by an increased surface roughness.

Moreover, in the C-2 sample, pronounced Kiessig oscillations in the high-angle region are observed (see the inset of Figure 3a), which allows the determination of the thickness of this sample to be approximately 80 nm. For the other samples, these oscillations are absent at higher 2θ values, which is most likely due to the formation of a number of larger holes in these films (larger surface roughness), as it can be seen

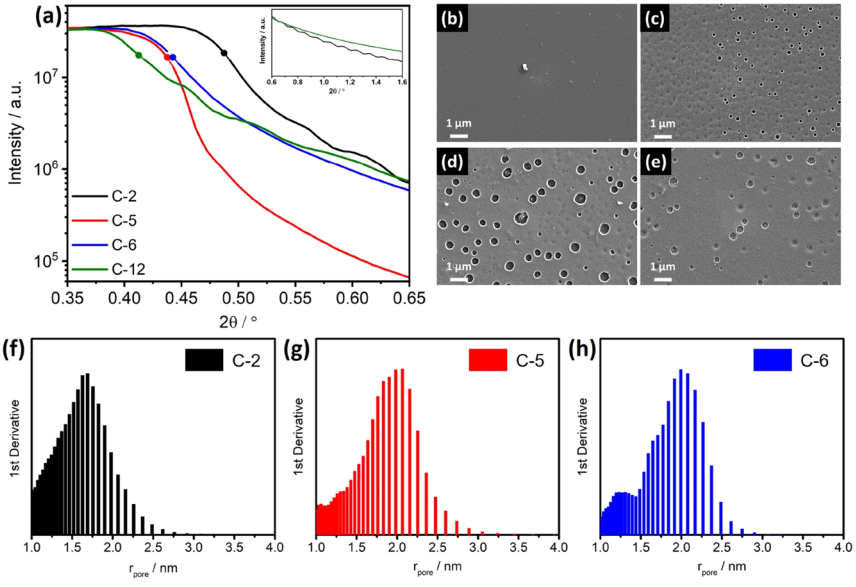

Figure 3. (a) XRR data and (b–e) SEM images of the ZnS films prepared by conversion of the zinc xanthate complexes on glass substrates after annealing at 400 °C (b: C-2, c: C-5, d: C-6, and e: C-12). Pore size distribution for (f) C-2, (g) C-5, and (h) C-6 films.

https://doi.org/10.1021/acsanm.1c04206
ACS Appl. Nano Mater. 2022, 5, 1508–1520

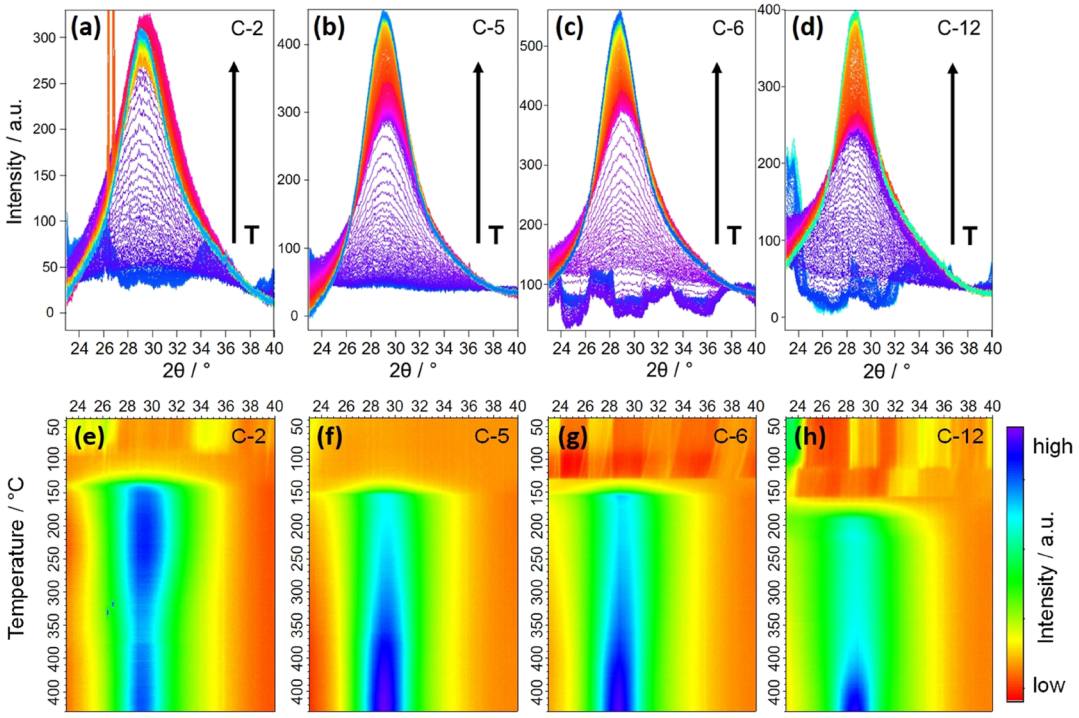

Figure 4. (a–d) GIWAXS patterns of thin films measured between 23.5 and 40° 2θ during heating runs from 37 up to 400 °C with a heating rate of 10 °C/min with a subsequent annealing time of 15 min, displaying the formation of the (111) reflection of ZnS. The increasing temperature (T) is indicated with a black arrow. (e–h) Corresponding surface plots of the investigated samples.

in the SEM images. In contrast to that, the surface of the C-2 film is homogeneous and smooth.

To support the assumption of increasing porosity of the ZnS films prepared from zinc xanthates with longer alkyl side chains, ellipsometric porosimetry (EP) was performed. EP is a type of adsorption porosimetry, which is based on traditional adsorption methods such as the Brunauer–Emmett–Teller porosimetry or Barrett–Joyner–Halenda analysis, and allows the determination of porosity and pore size distribution. Compared to the traditional methods that monitor the weight or differential pressure changes, EP uses the changes of optical properties, such as the refractive index, which occur during the adsorption and desorption of vapors, to define the amount of adsorption in the pores.[60]

The data obtained from the EP measurements of the samples were used for the calculation of the pore size distribution. Figure S9 shows the overall accessible porosity of the films with this specific measurement, which is 22, 31, and 47% for C-2, C-5, and C-6, respectively. The graph was obtained by plotting the volume adsorbed (eq S4) versus the relative humidity. Even though the C-12 sample could not be measured, according to the trend obtained from the three analyzed samples and the results from other measurements, we assume that the C-12 film is also highly porous.

Moreover, the pore size distribution was determined by differentiating the volume adsorbed–r_{pore} plots (Figure 3). The pore radius (r_{pore}) was calculated according to eq S3. The graphs show that the pore radii range between 1 and 4 nm, with most of them being between 1.2 and 2.5 nm, for all the samples. It should be noted that the applicability of Kelvin's equation is problematic at the nanoscale and pore sizes below approximately 1 nm.[61,62] In addition to the overall increasing porosity of the samples with higher alkyl chain lengths of the precursors, also the maximum of the pore size distribution is shifted to larger values.

To gain insights into the formation of the ZnS films with different porosities and pore sizes in the range of a few nanometers, the role of the alkyl ligands within this process was thoroughly investigated by time-resolved simultaneous GIWAXS and grazing incidence small-angle X-ray scattering (GISAXS) investigations. This revealed information about the formation of the nanocrystals, on the one hand, and about changes in the film structure, on the other hand. For this purpose, synchrotron radiation and a grazing incidence setup were used to study the temporal changes in the approximately 100 nm-thick films during a heating run from 37 to 400 °C (heating rate: 10 °C/min) with a time resolution of 6 s. At 400 °C, the samples were kept for 15 min to observe further potential changes under annealing conditions. The measurements were conducted under a nitrogen flow to resemble the laboratory conditions. These measurements together with the thermogravimetric analysis provide insight into the key processes within the formation of the markedly different nanoporosities of the films.

The GIWAXS measurements, performed in a 2θ range between 23.5 and 40°, allow to observe the evolution and changes of the (111) reflection of cubic ZnS during the heating run. The graphs in Figure 4 reveal that all the precursor films except C-5 display several narrow peaks at room temperature, which are due to partial crystallization of the metal xanthates in the precursor film after spin-coating. A similar behavior is also reported for Cd xanthates.[56] These peaks disappear shortly before the formation of the nanocrystalline ZnS starts, which indicates a melting process prior to the decomposition of the compounds. Moreover, the data, in particular, the surface plots shown in Figure 4e–h, show that the formation of the ZnS nanocrystals starts at different temperatures and also the

https://doi.org/10.1021/acsanm.1c04206
ACS Appl. Nano Mater. 2022, 5, 1508–1520

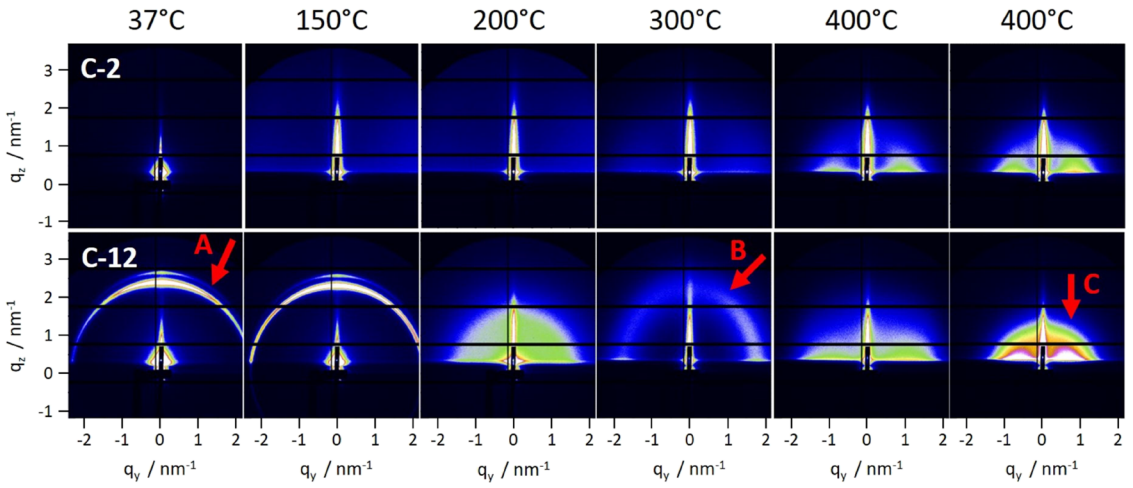

Figure 5. GISAXS patterns of the C-2 and C-12 samples at different temperatures starting from 37 up to 400 °C and 15 min annealing. Arrows A and B show semicircle-like features indicating a high order in the film. Arrow C displays the preferential near-range order of the ZnS nanoparticles in the in-plane direction.

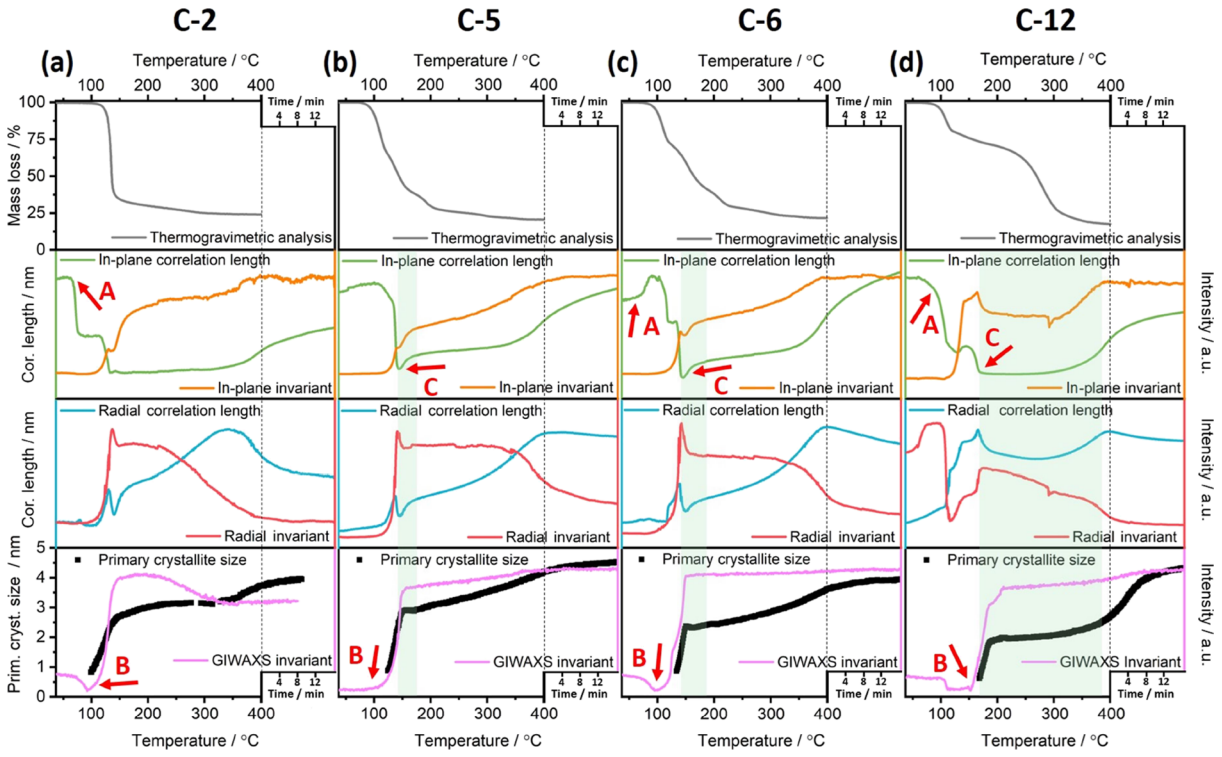

Figure 6. From top to bottom: TGA results (gray), in-plane correlation length (green) and invariant (orange), radial correlation length (blue) and invariant (red), and the GIWAXS invariant (pink) and the evolution of the primary crystallite size (black) during the heating run for (a) C-2, (b) C-5, (c) C-6, and (d) C-12. Arrows A, B, and C indicate the melting point, thermal conversion onset, and mesophase onset, respectively. The green areas indicate the presence of the ordered mesophase during the heating run. The dashed lines denote the beginning of annealing at a constant temperature (400 °C) for 15 min.

kinetics of the nanocrystal growth varies, which will be discussed in more detail in combination with the results of the simultaneously performed GISAXS measurements. The sharp peak visible in Figure 4a at a 2θ value of approximately 27° and at temperatures between 320 and 340 °C stems most presumably from an unknown crystal/impurity occasionally moving into the reflection conditions in this temperature range (see Figure 4e).

The GISAXS patterns of the four samples at different temperatures during the heating run are presented in Figure 5 (C-2 and C-12) and Figure S10 (C-5 and C-6). The in-plane and out-of-plane cuts and radial integration extracted from the GISAXS pattern demonstrating different aspects of the evolving structures, such as particle growth (in-plane), order across the film thickness (out-of-plane), and mesophase formation (radial direction) are shown in Figure S12. Qualitatively, the GISAXS data disclose that the samples bearing two, five, and six carbons on their alkyl ligand exhibit a rather similar behavior, while the C-12 sample significantly differs. In this sample, a distinct semicircle-like feature (arrow

https://doi.org/10.1021/acsanm.1c04206
ACS Appl. Nano Mater. 2022, 5, 1508−1520

A in Figure 5) is observed in addition to the scattering pattern expected for this type of samples indicating a high order in the film already after spin-coating. This scattering feature vanishes with the decomposition of the metal xanthates; however, a similar semicircle-like feature (arrow B in Figure 5) appears again at lower q-values at certain temperatures in the heating run at which the ZnS nanocrystals are already present. This reveals the formation of another preferential ordered phase within the nanocrystal film. Interestingly, this feature is not only seen in the C-12 sample, but also in the C-6 and to a lower extent even in the C-5 sample. Moreover, it is apparent that the GISAXS patterns show slight asymmetry with a higher intensity in the right part. We attribute this asymmetry to a preferential order of the precursors nonperpendicular to the substrate, which is also kept after the decomposition and conversion to the nanocrystalline ZnS films. In addition, the shape of the GISAXS patterns at 400 °C (arrow C in Figure 5) indicates a preferential near-range order of the ZnS nanoparticles in the in-plane direction and a loss of the near-range order in the out-of-plane direction in the final ZnS films.

Further analysis showed that during the temperature treatment, there were also distinct structural changes of the samples with shorter alkyl ligands implying a strong influence of the alkyl chain length not only on the formation process but also on the properties of the final ZnS film. Moreover, important information about changes in the samples occurring during the heating run can be gained from the evolution of the correlation length[63,64] and the Porod invariant with temperature and time extracted from the GISAXS (in-plane and radial integration, Figure S12) and the GIWAXS data. Here, the correlation length and the Porod invariant integrated over the limited q-range in the in-plane and radial cuts serve as a sensitive qualitative measure of the changes of the GISAXS patterns (see the Supporting Information). These parameters and the thermogravimetric analysis (TGA) data obtained from the powdered metal xanthates are presented in Figure 6.

The TGA analysis (Figure 6, top row) shows that the increasing alkyl chain length changes the decomposition and conversion processes. While the onset of decomposition (5% mass loss) is in a temperature range of 95 to 125 °C for all the compounds (C-2: 123 °C and C-5 to C-12: 95−100 °C), a second mass loss step becomes more pronounced and is shifted to higher temperatures with the increasing chain length of the alkyl moiety. For the C-12 sample, the onset of the second distinct mass loss step is even shifted to approximately 250 °C. This is due to the byproducts formed during the decomposition and their evaporation from the sample at higher temperatures. As already outlined in the Introduction Section, metal xanthates typically decompose according to the Chugaev elimination leading to COS and the respective alkene as products as well as an additional second process in which the volatile decomposition products are CS_2 and the respective alcohol.[30] Additionally, the pyridine ligand was found to be partly remaining as a ligand on the zinc ions, even at high temperatures, and thus also affecting the crystal growth.[30] Based on this, the potential byproducts, which are attributed to the structural changes, are the pyridine ligand for all the compounds and specifically ethene/ethanol for the C-2 sample, 1-pentene/1-pentanol for the C-5 sample, 1-hexene/1-hexanol for the C-6 sample, and 1-dodecene/1-dodecanol for the C-12 sample. While ethene and ethanol evaporate from the C-2 film directly at the decomposition temperature of the metal xanthate leading to the observed single-step mass loss, the onset of the second mass loss step in the C-5 to C-12 samples corresponds well with the boiling points of the respective alcohols formed as decomposition products (pentanol: 138 °C; hexanol: 158 °C; and dodecanol: 259 °C). Pentene and hexene have boiling points of 30 and 63 °C and thus also evaporate from the film directly at the decomposition temperature, while the boiling point of dodecene is 214 °C indicating that in the C-12 sample, in addition to dodecanol, dodecene also remains in the film for a significant amount of time during the heating run. This is also corroborated by the significantly lower mass loss in the first step in the C-12 sample (see Figure 6d).

In addition, the in-plane correlation length and invariant extracted from the GISAXS data (shown in the second row of Figure 6) provide evidence of distinct structural changes in all four samples taking place at the temperatures, where the main mass losses appear according to the TGA results. Based on the TGA, GIWAXS, and GISAXS data, the C-2 sample undergoes the following steps during the heating run: starting from 37 °C up to 95 °C, the metal xanthate is present. However, at 64 °C, a change is observed in the in-plane correlation length (arrow A in Figure 6), which is attributed to the compound's melting. At 95 °C, the thermal conversion starts (arrow B in Figure 6) and the first ZnS nanocrystals with an approximately 1 nm size are found at 101 °C. At the same time, the radial correlation length and invariant show a steep increase. At approximately 150 °C, the crystal growth continues with a significantly slower rate until a temperature of 352 °C, where the rate increases again.

In case of the C-5 sample, no peaks indicating a crystalline metal xanthate phase are observed. This is also in line with the fact that it was not possible to grow crystals of C-5 suitable for a single-crystal XRD measurement. The starting point of the thermal conversion at 102 °C and the first 1 nm size ZnS nanocrystals at 127 °C are followed as before by a steep increase of the GISAXS invariant corresponding to the increase in the volume fraction and electron density contrast due to the formation of the metal sulfide. At approximately 140 °C, the correlation length shows a minimum (arrow C in Figure 6) and a diffraction peak appears in the radial GISAXS pattern (Figure S12), suggesting the formation of an ordered mesophase in the film at this temperature (green area in Figure 6). The order of this mesophase is most pronounced at 153 °C (highest intensity, well-defined diffraction peak in the radial GISAXS pattern in Figure S14) and starts to fade at 168 °C.

The C-6 precursor is present in the film up to 98 °C, where the thermal conversion starts, while it also exhibits a melting process at 64 °C. The mesophase is formed at similar temperatures, as for C-5, but with a slightly longer duration. Lastly, even though the C-12 sample demonstrates the same steps, they are shifted to higher temperatures. The long presence of the mesophase is noteworthy as it appears at 171 °C and vanishes approximately at 381 °C. The temperatures of these key steps within the conversion for all four compounds are summarized in Table S7.

Next, we focused on the formation and properties of the mesophase by a deeper analysis of the GISAXS data. The GISAXS curves recorded at temperatures at which the mesophase is present in the C-5, C-6, and C-12 films (Figure S14) reveal that the mesophase diffraction peak is found at different temperature ranges and at different q_r values between 2.9 and 1.9 nm^{-1} (Figure S14). This suggests that its formation is attributed to distinct compounds. By fitting the frame with

https://doi.org/10.1021/acsanm.1c04206
ACS Appl. Nano Mater. 2022, 5, 1508−1520

Table 1. Properties of the Observed Mesophase at the Point of Its Highest Intensity in the Radial GISAXS Curves

	C-2	C-5	C-6	C-12
temperature/°C	no ordered mesophase	153	155	221
peak position q_r/nm^{-1}		2.14 ± 0.01	2.09 ± 0.01	1.79 ± 0.01
FWHM/nm^{-1}[a]		0.34 ± 0.01	0.47 ± 0.01	0.32 ± 0.01
particle−particle distance, D/nm		2.94 ± 0.01	3.01 ± 0.01	3.48 ± 0.02
primary crystallite size/nm[b]		2.84 ± 0.03	2.37 ± 0.02	1.97 ± 0.02
size of intermediate features in the mesophase/nm[c]		0.10 ± 0.04	0.64 ± 0.03	1.51 ± 0.04

[a]FWHM determined from the peak in the GISAXS pattern by fitting a Lorentzian peak shape. [b]Estimated using the Scherrer equation from the FWHM of the (111) reflection in the GIWAXS data (the given error represents the uncertainty based on the determination of the FWHM). [c]Calculated from the particle−particle distance and the primary crystallite size.

Table 2. Particle−Particle Distances and Particle and Pore Sizes in the Final ZnS Films (after 15 min Heating at 400 °C) Determined from the GISAXS and GIWAXS Data

	C-2	C-5	C-6	C-12
maximum of the scattering curve (q_r-value)/nm^{-1}	0.87 ± 0.01	0.83 ± 0.01	0.79 ± 0.01	0.66 ± 0.01
particle−particle distance, D/nm[a]	7.22 ± 0.07	7.57 ± 0.07	7.95 ± 0.08	9.52 ± 0.12
mean diameter of Schulz distributed spheres/nm[b]	3.34 ± 0.14	3.42 ± 0.06	3.84 ± 0.04	3.94 ± 0.01
polydispersity[c]	0.24 ± 0.04	0.16 ± 0.02	0.14 ± 0.01	0.21 ± 0.01
primary crystallite size/nm[d]	3.74 ± 0.05	4.10 ± 0.06	4.04 ± 0.04	4.32 ± 0.05
size of the intermediate features/nm[e]	3.88 ± 0.11	4.15 ± 0.08	4.12 ± 0.09	5.58 ± 0.12

[a]Calculated from the maxima of the scattering curves ($D = 2\pi/q_r$) at the end of the heating run. [b]From fitting of the full scattering curve. [c]Standard deviation divided by the mean size. [d]Estimated using the Scherrer equation from the FWHM of the 111 peak from the GIWAXS data (the given error represents the uncertainty based on the determination of the FWHM). [e]Difference of the particle−particle distance and mean diameter of Schulz distributed spheres.

the maximum intensity of the ordered mesophase with a Lorentz function, we determined the peak position q_r, of which the mean distance between the scattering features D has been calculated ($D = 2\pi/q_r$).

The scattering features in that case are the ZnS nanocrystals and their size can be extracted from the GIWAXS measurements and the evolution of the primary crystallite size. The subtraction of the crystallite size from the calculated D values for the temperature at which the maximum ordered mesophase is obtained yields the size of intermediate features. Table 1 summarizes the corresponding particle sizes and distances. These results illustrate that the size of the intermediate features increases with the increasing length of the alkyl chain of the precursor, indicating that the alkyl ligand plays a primary role in the process. Particularly, in case of C-12, the size of 1.51 nm fits very well with the length of the dodecyl side chain, which is 1.5 nm between the oxygen O1 or O2 and carbon C18 or C31, respectively, according to the crystal structure (Figure S3). This suggests that the decomposition products (dodecene and dodecanol) are responsible for the mesophase formation. This result also fits well with the TGA (vide supra) and the boiling points of these compounds.[65] Similarly, the size of 0.64 nm matches well with the length of the hexyl side chain between O1 and C7 (0.68 nm) and O2 and C14 (0.69 nm), respectively, according to the crystal structure (Figure S3). As a result, 1-hexanol, also by taking into account its thermal stability (b.p. 157 °C),[66] is responsible for the mesophase formation. In the other two cases, the situation is slightly different. While in the C-2 sample, due to the high volatility of the decomposition products ethene and ethanol, no ordered mesophase is observed, and the C-5 sample reveals a mesophase with a low order present only in a short time frame. Moreover, in this case, the size of the intermediate feature is only 0.1 nm (see Table 1) and thus we assume that in this sample, the mesophase is formed due to the presence of the pyridine ligands, which remain capped on the metal center also at higher temperatures rather than the decomposition products pentene and pentanol.

Hence, we can conclude that the longer the alkyl ligand, the more likely is the formation of an ordered lamellar mesophase.[67,68] Furthermore, the degree of order is revealed by the width of the respective peak in the GISAXS pattern (Table 1, full width half maximum (FWHM)). In this regard, the C-12 sample shows the highest order, while the C-6 and C-5 samples reveal a lower one. Moreover, the GISAXS data (Figure S13) reveal that the ZnS nanocrystals have a preferred vertical orientation, with the above-discussed decomposition products arranged in between the nanoparticles in a lamellar configuration.

The removal of the byproducts due to the increasing temperature and thus the disappearance of the mesophase lead to an overall structure collapse, as illustrated in the final frames in Figures 5 and S10. The calculation of the particle−particle distance from eq 5 using the q_r-value corresponding to the maximum of the last scattering curve measured in the heating run (400 °C, in-plane integration) and additional fitting of the curve reveals detailed information about the structure of the final film. As only relative changes between the samples were the main focus of this analysis of the GISAXS data, a simplified, analytical approach rather than the full use of the DWBA theory[69,70] has been applied. For the fitting of the 2D GISAXS patterns, only in-plane cuts were analyzed with a simplified structural model including form factor scattering and a structure factor contribution. More details about this model and the obtained fits together with the in-plane cuts are shown in the Supporting Information (Figures S15 and S16).

The fits of the full scattering curves reveal the mean diameter of Schulz distributed spheres, which matches well with the primary crystallite size extracted from the GIWAXS data, taking into account the uncertainties in the estimation of

https://doi.org/10.1021/acsanm.1c04206
ACS Appl. Nano Mater. 2022, 5, 1508−1520

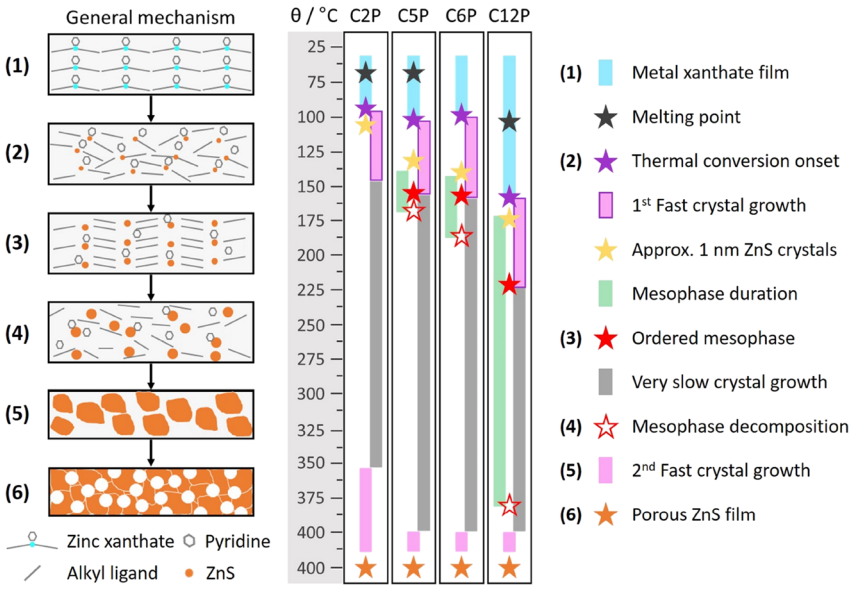

Figure 7. General mechanism with important steps (left), the overall process with the temperatures and durations for each compound (middle), and the respective information (right).

the primary crystallite sizes via the Scherrer equation (see Table 2). The sizes of the intermediate features corresponding to the pore diameters are calculated via the particle−particle distance and the mean diameter of the Schulz distributed spheres (Figure S17) and they reveal values increasing from 3.88 nm (C-2) to 5.58 nm (C-12), which fit well with the pore radius distributions determined by the EP measurements (Figure 3). Moreover, comparatively small polydispersities between 0.14 and 0.24 are observed. This is notably taking into account that the nanocrystals are formed directly in the film in a solvent-free route; however, we assume that the second fast growth phase of the nanocrystals between 350 and 400 °C (see the last row of Figure 6, evolution of the primary crystallite size) is based on an Ostwald ripening-type growth mechanism during which the particle size distribution is expected to be narrowed.

CONCLUSIONS

In conclusion, this study reports a facile route toward nanoporous zinc sulfide thin films based on the thermal conversion of metal xanthate precursors. Thereby, the design of the alkyl ligand of the xanthate groups plays an important role in controlling the creation of the porosity of the films as the length of the alkyl ligand significantly affects the conversion and the formation processes of the nanocrystalline zinc sulfide films. With an increasing number of carbons in the alkyl chain, the overall porosity and the pore size in the range of a few nanometers are significantly enhanced. Based on an in-depth analysis of the film formation process, we found that the conversion of the metal xanthate precursors to the nanoporous zinc sulfide films is based on the mechanism outlined in Figure 7.

After spin-coating, the metal xanthates typically form a crystalline film (1) on the substrate, and upon heating, the metal xanthate films melt a few tens of degrees before the onset of the thermal decomposition (2). Subsequently, a first fast crystal growth is experienced and approximately 1 nm-sized nanocrystals are obtained at 110 °C in the C-2 sample. For precursors with longer alkyl chains, this temperature increases and for the C-12 sample, 1 nm ZnS particles are found at 170 °C. Additionally, it is very interesting to note that a lamellar mesophase (3), which is formed by the decomposition products of the metal xanthates, is obtained in a certain temperature range during the thermal conversion process. The longer the alkyl chain of the xanthates, the more ordered is also the observed mesophase and the temperature range at which this ordered mesophase starts to disappear (4) corresponds well with the boiling points of the respective byproducts. The presence of the mesophase also causes a very slow crystal growth, which becomes faster again once the ordered lamellar phase has dissipated. Moreover, as the byproducts are present in the film in an ordered lamellar phase before they evaporate from the film, the nanoporosity is strongly influenced and determined by their size, which can be exploited to tune the pore sizes and the overall porosity of the films. While in the C-2 sample, pore sizes of 3.9 nm are found, the C-12 sample exhibits markedly larger pore sizes of 5.6 nm.

The ability to form nanoporous metal sulfide films, as well as to control their porosity by simply using metal xanthate precursors, is a cost-effective, efficient, and scalable process due to the absence of complicated templating procedures and sophisticated equipment. In addition, as this straightforward route toward porous metal sulfide thin films can be used for a plethora of metal sulfides, and consequently, can enhance their performance in a wide range of applications, we anticipate that the presented method will be a valuable tool for the formation of metal sulfide films with defined nanoporosity in the future. As these films can be particularly well suited for photocatalytic applications, we envisage to apply the developed method toward the preparation of nanoporous nickel sulfide films and to investigate their photocatalytic properties in water splitting applications in future research.

EXPERIMENTAL SECTION

Materials and Methods. All chemicals and solvents were purchased and used without any additional purification (except potassium ethyl xanthogenate): chloroform (≥99.2%, VWR), methanol (VWR), diethyl ether (≥99.5%, Sigma-Aldrich), acetone (≥99%, Sigma-Aldrich), deuterium oxide (Eurisotop), deuterated

https://doi.org/10.1021/acsanm.1c04206
ACS Appl. Nano Mater. 2022, 5, 1508−1520

chloroform (99.8 atom % *D*, 0.03% (v/v) TMS, Eurisotop), dimethyl sulfoxide (DMSO-d_6, 0.03% (v/v) TMS, Eurisotop), potassium hydroxide (VWR), potassium *tert*-butoxide (≥98%, Sigma-Aldrich), potassium ethyl xanthogenate (96%, Sigma-Aldrich), hexanol-1 (anhydrous, ≥99%, Sigma-Aldrich), pentanol-1 (98%, Fluka AG), dodecanol-1 (97%, Fluka AG), carbon disulfide (≥99.9%, Sigma-Aldrich), zinc chloride (≥98%, Sigma-Aldrich), and pyridine (≥99%, Sigma-Aldrich).

Potassium *O*-alkyl-1-yl-dithiocarbonate (KXaCx). All KXaCx (apart from KXaC2) compounds were obtained using adapted procedures.[71,72] KXaC2 was commercially available (potassium xanthogenate). Therefore, it was purified before its use for the synthesis by dissolving in acetone and precipitating in diethyl ether followed by collecting the precipitate through filtration and subsequent drying under vacuum. For the synthesis of KXaC5 and KXaC6, potassium hydroxide (53.0 mmol, 1.0 equiv) was added and partly dissolved in the respective alcohol (1-pentanol, 1-hexanol, 58.3 mmol, 1.1 equiv) under stirring. The mixtures were cooled down to 0 °C and CS_2 (58.3 mmol, 1.1 equiv) was added dropwise under stirring. The resulting slurry was stirred for 30 min and washed with diethyl ether. In the case of KXaC12, potassium *tert*-butoxide (30.3 mmol, 1.0 equiv) was dissolved in dry THF under inert conditions (N_2). The mixture was then cooled down to 0 °C and 1-dodecanol (33.3 mmol, 1.1 equiv) was added slowly. After stirring for several minutes, CS_2 (2.5 g, 33.3 mmol, 1.1 equiv) was added dropwise. The solution was stirred for 3 h under N_2 at 0 °C. All products were collected by filtration and dried under vacuum at room temperature. Finally, the dry products were dissolved in acetone and precipitated in diethyl ether in order to obtain a pure yellowish product.

KXaC2. ^{1}H NMR (300 MHz, $CDCl_3$): δ = 4.51−4.44 (q, 2H, CH_2), 1.35 (t, 3H, CH_3). ^{13}C NMR (76 MHz, $CDCl_3$): δ = 232.8 (CS_2O), 70.3 (CH_2), 13.6 (CH_3). FTIR (v/cm^{-1}): 2983, 2968, 2889, 1463, 1381, 1171, 1136, 1096, 1067, 1045.

KXaC5. ^{1}H NMR (300 MHz, D_2O): δ = 4.46 (t, 2H, CH_2), 1.79−1.75 (m, 2H, CH_2), 1.39−1.38 (m, 4H, 2× CH_2), 0.92 (t, 3H, CH_3). ^{13}C NMR (76 MHz, D_2O): δ = 233.1 (CS_2O), 74.6 (CH_2), 27.8 (CH_2), 27.6 (CH_2), 21.7 (CH_2), 13.3 (CH_3). FTIR (v/cm^{-1}): 2956, 2924, 2854, 1459, 1379, 1208, 1163, 1134, 1110, 1067, 1040.

KXaC6. ^{1}H NMR (300 MHz, D_2O): δ = 4.46 (t, 2H, CH_2), 1.78−1.72 (m, 2H, CH_2), 1.42−1.33 (m, 6H, 3× CH_2), 0.89 (t, 3H, CH_3). ^{13}C NMR (76 MHz, D_2O): δ = 230.1 (CS_2O), 74.6 (CH_2), 30.8 (CH_2), 28.0 (CH_2), 24.9 (CH_2) 21.9 (CH_2), 13.3 (CH_3). FTIR (v/cm^{-1}): 2952, 2922, 2854, 1465, 1379, 1200 1165, 1136, 1071, 1032.

KXaC12. ^{1}H NMR (300 MHz, DMSO-d_6): δ = 4.16 (t, 2H, CH_2), 1.55−1.53 (m, 2H, CH_2), 1.24 (s, 18H, 9× CH_2), 0.84 (t, 3H, CH_3). ^{13}C NMR (76 MHz, DMSO-d_6): δ = 230.0 (CS_2O), 70.5 (CH_2), 31.3 (CH_2), 30.7−22.1 (9× CH_2), 13.9 (CH_3). FTIR (v/cm^{-1}): 2954, 2911, 2848, 1470, 1379, 1200, 1165, 1138, 1108, 1071, 1047.

Zinc(II)-*O*-alkyl-dithiocarbonate (ZnXaCx). The syntheses of all ZnXaCx compounds are based on previous studies.[48,54] Zinc(II) chloride (1.0 equiv) was dissolved in 50 mL of deionized water (or methanol for the synthesis of ZnXaC12). KXaCx (2.1 equiv) was first dissolved in 75 mL of deionized water (or methanol for the synthesis of ZnXaC12) and was subsequently added dropwise to the first solution under stirring. A white solid was immediately formed after the addition. After 2 h of stirring at room temperature under ambient conditions, the solid material was filtrated and dried under vacuum.

ZnXaC2. ^{1}H NMR (300 MHz, $CDCl_3$): δ = 4.60−4.53 (q, 2H, CH_2), 1.47 (t, 3H, CH_3). ^{13}C NMR (76 MHz, $CDCl_3$): δ = 230.1 (CS_2O), 73.9 (CH_2), 14.1 (CH_3). FTIR (v/cm^{-1}): 2991, 2938, 2885, 1467, 1383, 1206, 1187, 1145, 1120, 1067, 1047.

ZnXaC5. ^{1}H NMR (300 MHz, $CDCl_3$): δ = 4.48 (t, 2H, CH_2), 1.82 (s, 2H, CH_2), 1.38−1.37 (d, 4H, 2× CH_2), 0.91 (t, 3H, CH_3). ^{13}C NMR (76 MHz, $CDCl_3$): δ = 230.2 (CS_2O), 78.4 (CH_2), 28.2 (CH_2), 28.0 (CH_2), 22.4 (CH_2), 14.0 (CH_3). FTIR (v/cm^{-1}): 2950, 2868, 2917, 2858, 1465, 1375, 1212, 1189, 1142, 1128, 1069, 1036.

ZnXaC6. ^{1}H NMR (300 MHz, $CDCl_3$): δ = 4.49 (t, 2H, CH_2), 1.85−1.80 (d, 2H, CH_2), 1.42−1.32 (m, 6H, 3× CH_2), 0.90 (t, 3H, CH_3). ^{13}C NMR (76 MHz, $CDCl_3$): δ = 230.3 (CS_2O), 78.4 (CH_2), 31.5 (CH_2), 28.5 (CH_2), 25.6 (CH_2), 22.6 (CH_2), 14.1 (CH_3). FTIR (v/cm^{-1}): 2952, 2911, 2848, 1463, 1377, 1234, 1208, 1189, 1142, 1128, 1077, 1043.

ZnXaC12. ^{1}H NMR (300 MHz, $CDCl_3$): δ = 4.49 (t, 2H, CH_2), 1.83 (t, 2H, CH_2), 1.25 (s, 18H, 9× CH_2), 0.87 (t, 3H, CH_3). ^{13}C NMR (76 MHz, $CDCl_3$): δ = 230.3 (CS_2O), 78.5 (CH_2), 32.1 (CH_2), 29.8−22.8 (9× CH_2), 14.3 (CH_3). FTIR (v/cm^{-1}): 2952, 2915, 2846, 1463, 1377, 1203, 1198, 1147, 1130, 1102, 1065, 1046.

Pyridine Zinc(II)-*O*-alkyl-dithiocarbonate (ZnXaCxP). The synthesis of ZnXaCxP was based on the procedure reported in ref 58. ZnXaCx (1.0 equiv) was dissolved in methanol (20 mL/mmol). When a clear solution was formed, pyridine (266 μL, 1.0 equiv, 3.3 mmol) was added and stirred. In the case of ZnXaC2P, a white solid precipitate was formed and stirred for 2 h at room temperature under ambient conditions. For ZnXaC5P and ZnXaC6P, after the addition of pyridine, the clear yellow solution was added dropwise in water, forming an emulsion. The emulsion was stirred for 3 h at room temperature under ambient conditions, leading to the precipitation of a white solid. Finally, for the synthesis of ZnXaC12P, a completely different process was followed. The compound ZnXaC12 (1.0 equiv) was dissolved in chloroform. Under stirring, pyridine (1.0 equiv) was added, leading to a clear solution. After stirring for 2 h, the solution was added in stirring methanol, where a white solid was precipitated. In all cases, the white solids were collected by filtration and dried under vacuum.

ZnXaC2P. ^{1}H NMR (300 MHz, $CDCl_3$): δ = 8.96−8.94 (d, 2H, 2× CH, pyridine), 8.02 (t, 1H, CH, pyridine), 7.61 (t, 2H, 2× CH, pyridine), 4.54−4.47 (q, 2H, CH_2), 1.44 (t, 3H, CH_3). ^{13}C NMR (76 MHz, $CDCl_3$): δ = 230.0 (CS_2O), 149.2 (CH, pyridine), 140.3 (2× CH, pyridine), 125.7 (2× CH, pyridine) 73.2 (CH_2), 14.2 (CH_3). FTIR (v/cm^{-1}): 2979, 2934, 2893, 1606, 1483, 1469, 1446, 1387, 1200, 1147, 1114, 1065, 1038.

ZnXaC5P. ^{1}H NMR (300 MHz, $CDCl_3$): δ = 8.95−8.94 (d, 2H, 2× CH, pyridine), 8.01 (t, 1H, CH, pyridine), 7.60 (t, 2H, 2× CH, pyridine), 4.43 (t, 2H, CH_2), 1.83−1.79 (m, 2H, CH_2), 1.38−1.37 (m, 4H, 2× CH_2), 0.91 (t, 3H, CH_3). ^{13}C NMR (76 MHz, $CDCl_3$): δ = 230.2 (CS_2O), 149.2 (CH, pyridine), 140.2 (2× CH, pyridine), 125.7 (2× CH, pyridine) 70.7 (CH_2), 28.3 (CH_2), 28.1 (CH_2), 22.4 (CH_2), 14.0 (CH_3). FTIR (v/cm^{-1}): 2956, 2928, 2858, 1608, 1487, 1469, 1446, 1377, 1212, 1198, 1140, 1126, 1063, 1043.

ZnXaC6P. ^{1}H NMR (300 MHz, $CDCl_3$): δ = 8.97−8.95 (d, 2H, 2× CH, pyridine), 8.02 (t, 1H, CH, pyridine), 7.61 (t, 2H, 2× CH, pyridine), 4.43 (t, 2H, CH_2), 1.85−1.76 (m, 2H, CH_2), 1.44−1.31 (m, 6H, 3× CH_2), 0.89 (t, 3H, CH_3). ^{13}C NMR (76 MHz, $CDCl_3$): δ = 230.3 (CS_2O), 149.1 (CH, pyridine), 140.3 (2× CH, pyridine), 125.6 (2× CH, pyridine) 70.6 (CH_2), 31.4 (CH_2), 28.4 (CH_2), 25.5 (CH_2), 22.5 (CH_2), 14.0 (CH_3). FTIR (v/cm^{-1}): 2952, 2919, 2854, 1605, 1485, 1465, 1446, 1375, 1193, 1140, 1126, 1073, 1045.

ZnXaC12P. ^{1}H NMR (300 MHz, $CDCl_3$): δ = 8.95−8.94 (d, 2H, 2× CH, pyridine), 8.00 (t, 1H, CH, pyridine), 7.60 (t, 2H, 2× CH, pyridine), 4.43 (t, 2H, CH_2), 1.83−1.78 (m, 2H, CH_2), 1.25 (s, 18H, 9× CH_2), 0.86 (t, 3H, CH_3). ^{13}C NMR (76 MHz, $CDCl_3$): δ = 229.7 (CS_2O), 148.7 (CH, pyridine), 139.7 (2× CH, pyridine), 125.2 (2× CH, pyridine), 70.2 (CH_2), 31.6 (CH_2), 29.3−22.3 (9× CH_2), 13.8 (CH_3). FTIR (v/cm^{-1}): 2952, 2913, 2848, 1606, 1483, 1471, 1446, 1375, 1208, 1198, 1147 1128, 1104, 1065, 1046.

Film Formation. Zinc sulfide thin films were prepared via spin-coating and subsequent thermal decomposition of the precursors ZnXaC2P, ZnXaC5P, ZnXaC6P, and ZnXaC12P on silicon wafers and glass substrates (15 mm × 15 mm). The substrates were cleaned by sonication in isopropanol for 40 min at 40 °C and by treatment with oxygen plasma for 3 min (Femto low-pressure plasma system, Diener electronic). The precursors were dissolved in chloroform with a concentration of 100 mg/mL. The solutions were filtered using syringe filters and deposited on the substrates. The spin-coating was performed at 1000 rpm for 30 s, and then the substrates were placed in an oven to be dried under a N_2 flow at room temperature. Subsequently, the temperature was raised to 400 °C (10 °C/min) and kept at that temperature for 15 min under a continuous N_2 flow.

https://doi.org/10.1021/acsanm.1c04206
ACS Appl. Nano Mater. 2022, 5, 1508−1520

Finally, the layers were cooled down to room temperature under the N_2 flow.

Characterization Techniques. NMR spectra were recorded using a Bruker Ultrashield 300 MHz NMR spectrometer (^{1}H NMR: 300 MHz and ^{13}C NMR: 75 MHz). The solvents used were deuterated chloroform with tetramethylsilane (TMS) (^{1}H NMR: 7.26 ppm and ^{13}C NMR: 77.16 ppm), deuterium oxide (^{1}H NMR: 4.79 ppm), and DMSO-d_6 with tetramethylsilane (TMS) (^{1}H NMR: 2.50 ppm and ^{13}C NMR: 39.52 ppm).[73] The spectra were evaluated with TopSpin 3.1 from Bruker. The chemical shifts are given in units of the δ scale in parts per million (ppm).

FTIR spectra were measured using a Bruker Alpha FTIR spectrometer in the attenuated total reflection (ATR) mode using the ALPHA's Platinum ATR single-reflection diamond ATR module and in the transmission mode (layers on silicon wafers). All spectra were recorded in a range between 4000 and 400 cm^{-1} with 24 scans and air as background for the ATR mode and a blank silicon wafer for the transmission mode.

TG measurements were performed using a Netzsch Jupiter STA 449C thermogravimetric analyzer in aluminum oxide crucibles under a helium atmosphere with a flow rate of 50 mL/min. The operated temperature range was between 20 and 550 °C with a heating rate of 10 °C/min.

For the single-crystal XRD measurements, crystals of ZnXaC6P and ZnXaC12P were obtained as described below. The ZnXaC2P crystal structure was already known from the literature and recrystallization of compound ZnXaC5P did not yield good quality crystals with any method used. Crystals of ZnXaC6P were obtained by the slow evaporation of the solvent, whereas the ZnXaC12P crystals were obtained by using the antisolvent method. The zinc xanthates were dissolved in chloroform and filtered using a 0.2 μm filter to remove any impurities. The ZnXaC6P solution was kept in a beaker and left undisturbed until the solvent was evaporated. The ZnXaC12P solution was placed in a glass vial and covered with a paraffin film, which was pierced with a needle. The glass vial was placed in a sealable screw vessel, which had previously been filled in the bottom with the antisolvent (methanol). The crystals were formed at room temperature.

All crystals suitable for single-crystal XRD were removed from a vial or a Schlenk and immediately covered with a layer of silicone oil. A single crystal was selected, mounted on a glass rod on a copper pin, and placed in the cold N_2 stream provided by an Oxford Cryosystems cryostream. XRD data collection was performed for all compounds on a Bruker APEX II diffractometer[74] using an IμS microsource (Incoatec Microfocus) sealed tube of Mo Kα radiation (λ = 0.71073 Å) and a CCD area detector. The unit cell constants and the orientation matrices were determined by the program CELL_NOW.[75] Data integration was carried out using SAINT.[74] Empirical absorption corrections were applied using SADABS.[76,77] The structures were solved using the intrinsic phasing option in SHELXT[78] and refined by the full-matrix least-squares procedures in SHELXL[78−82] as implemented in the program SHELXLE.[83] The space group assignments and structural solutions were evaluated using PLATON.[84,85] Nonhydrogen atoms were refined anisotropically. Hydrogen atoms were located in calculated positions corresponding to the standard bond lengths and angles. In ZnXaC12P, similar ADP restraint SIMU was used in order to make the ADP values of problematic atoms more reasonable. In some tough cases, anisotropic U^{ij} values of the atoms were restrained (ISOR) to behave more isotropically. All crystal structure representations were made with the program Diamond[86] with all noncarbon atoms displayed as 30% ellipsoids. CIF files were edited, validated, and formatted either with the program publCIF[87] or Olex2.[88] CCDC 2112481 and 2112482 contain the supplementary crystallographic data for compounds ZnXaC6P and ZnXaC12P, respectively. These data can be obtained free of charge from The Cambridge Crystallographic Data Centre via www.ccdc.cam.ac.uk/data_request/cif. Table S3 contains crystallographic data and details of measurements and refinement for compounds ZnXaC6P and ZnXaC12P.

The layer thickness was determined using a Bruker Dektak XT stylus profilometer equipped with a 12.5 μm-radius stylus tip. The line scans were conducted over a length of 1000 μm with a stylus force of 3 mg.

XRR was carried out with a PANalytical Empyrean reflectometer using Cu Kα radiation. An X-ray mirror was used for parallelizing and monochromatizating the primary X-ray beam. At the diffracted beam side, an antiscatter slit and a 0.02 rad Soller slit were used together with a PIXcel3D detector operating as a point detector. The electron densities were calculated from the critical angle of total external reflection (θ_C) taken at the incidence angle θ showing half of the maximum intensity value. The Kiessig fringes were evaluated in terms of film thickness.

The SEM investigations were carried out using a ZEISS Ultra 55 field-emission scanning electron microscope in high vacuum. In order to characterize the surfaces of the thin zinc sulfide layers morphologically, the imaging was carried out in a low-energy range (3 keV excitation energy, secondary electron imaging with the SEI detector = Inlens detector). The ZnS layers were coated with a 10−15 nm thin layer of ultrapure carbon in a carbon filament evaporation plant, which enabled high-quality imaging without obscuring the actual contrasts of the zinc sulfide surface.

EP was performed using a spectroscopic ellipsometer (J.A. Woollam M-2000 V), equipped with a temperature stage (THMS600), at an angle of 75° and at wavelengths of 370−1000 nm. Analysis was carried out using the software CompleteEASE in which a three-layer model was applied, consisting of a silicon substrate, a native silicon oxide layer with a fixed thickness of 1.5−2 nm, and a Cauchy layer:

$$n(\lambda) = A + \frac{B}{\lambda^2} + \frac{C}{\lambda^4}$$

where n is the wavelength-dependent refractive index, λ is the wavelength, and A, B, and C are the fit parameters. Thus, the thickness and refractive index of the sample could be reported at every measurement step.

The temperature stage was connected to a custom-built mixing setup, which allowed for tuning the relative humidity in the measurement chamber from 0 to 85%. A dry atmosphere (i.e., 0% relative humidity) was reached using a N_2 flow, removing water from the measurement chamber. To increase the relative humidity, the N_2 flow was mixed with humid air and adjusted in equilibrium steps, which was monitored via a sensor in the measurement chamber (SparkFun SHT-15). The temperature of the stage was kept at room temperature, ensuring that the measured relative humidity in the chamber was the same as on top of the samples. In this way, pores with a diameter ≥0.33 nm (the kinetic diameter of the water molecules) were probed.

Simultaneous GISAXS and GIWAXS measurements were performed at the Austrian SAXS beamline 5.2L of the electron storage ring, Elettra (Italy).[89] The setup was adjusted to a q-range ($q = 4\pi/\lambda\sin(2\theta/2)$) between 0.1 and 3.5 nm^{-1} (GISAXS) and the angular range (2θ) between 23.5 and 40.0° (GIWAXS). The measurements were performed at a photon energy of 8 keV. The samples were mounted on an Anton Paar DHS 1100 heating stage using clamps to assure good thermal contact of the sample with the heating cell. The heating cell was equipped with a specially designed dome having Kapton windows to provide high X-ray transmissivity and low background. The GIWAXS signal was monitored using a Dectris Pilatus 100 K detector and the GISAXS signal with a Dectris Pilatus3 1 M detector. The angular calibration of the detectors was carried out using p-bromobenzoic acid and silver behenate powder (d-spacing of 58.38 Å), respectively. The sample chamber was purged with nitrogen flow during the whole experiment. The temperature range used was from 37 up to 400 °C with a heating rate of 10 °C/min. A temperature resolution of 1 °C could be obtained by having one frame every 6 s (5 s exposure). All measurements have been performed with a grazing angle of 0.25°. The off-specular out-of-plane integration was conducted in a q-range between 0.07 and 0.17 nm^{-1}, the in-plane integration between 0.31 and 0.41 nm^{-1}, and the radial

https://doi.org/10.1021/acsanm.1c04206
ACS Appl. Nano Mater. 2022, 5, 1508−1520

integration in an area as indicated in Figure S11b and they have been calculated with the data evaluation software SAXS DOG.[90]

■ ASSOCIATED CONTENT

Supporting Information

The Supporting Information is available free of charge at https://pubs.acs.org/doi/10.1021/acsanm.1c04206.

FTIR and NMR spectra, single-crystal, powder XRD, and TGA data, additional characterizations of the nanoporous ZnS films (FTIR spectra, XRR, SEM, EP, GIWAXS, and GISAXS), and information about the performed data analyses (PDF)

■ AUTHOR INFORMATION

Corresponding Authors

Thomas Rath − *Institute for Chemistry and Technology of Materials (ICTM), NAWI Graz, Graz University of Technology, Graz 8010, Austria;* orcid.org/0000-0002-4837-7726; Email: thomas.rath@tugraz.at

Heinz Amenitsch − *Institute of Inorganic Chemistry, NAWI Graz, Graz University of Technology, Graz 8010, Austria;* Email: amenitsch@tugraz.at

Authors

Efthymia Vakalopoulou − *Institute for Chemistry and Technology of Materials (ICTM), NAWI Graz, Graz University of Technology, Graz 8010, Austria;* orcid.org/0000-0002-9319-5200

Marianne Kräuter − *Institute of Solid State Physics, NAWI Graz, Graz University of Technology, Graz 8010, Austria*

Ana Torvisco − *Institute of Inorganic Chemistry, NAWI Graz, Graz University of Technology, Graz 8010, Austria;* orcid.org/0000-0002-6203-7330

Roland C. Fischer − *Institute of Inorganic Chemistry, NAWI Graz, Graz University of Technology, Graz 8010, Austria;* orcid.org/0000-0001-9523-5010

Birgit Kunert − *Institute of Solid State Physics, NAWI Graz, Graz University of Technology, Graz 8010, Austria*

Roland Resel − *Institute of Solid State Physics, NAWI Graz, Graz University of Technology, Graz 8010, Austria;* orcid.org/0000-0003-0079-3525

Hartmuth Schröttner − *Institute of Electron Microscopy and Nanoanalysis, Graz University of Technology, Graz 8010, Austria*

Anna Maria Coclite − *Institute of Solid State Physics, NAWI Graz, Graz University of Technology, Graz 8010, Austria;* orcid.org/0000-0001-5562-9744

Gregor Trimmel − *Institute for Chemistry and Technology of Materials (ICTM), NAWI Graz, Graz University of Technology, Graz 8010, Austria;* orcid.org/0000-0001-8922-4163

Complete contact information is available at: https://pubs.acs.org/10.1021/acsanm.1c04206

Author Contributions

The manuscript was written through contributions of all authors. All authors have given approval to the final version of the manuscript.

Funding

Graz University of Technology - Lead Project Porous Materials at Work (LP-03); CERIC-ERIC Consortium.

Notes

The authors declare no competing financial interest.

■ ACKNOWLEDGMENTS

The authors gratefully acknowledge Graz University of Technology for financial support through the Lead Project Porous Materials at Work (LP-03) as well as Josefine Hobisch for the support regarding the TGA. Moreover, the authors acknowledge the CERIC-ERIC Consortium for the access to experimental facilities (Austrian SAXS beamline at Elettra Sincrotrone Trieste) and financial support.

■ REFERENCES

(1) Innocenzi, P.; Malfatti, L. Mesoporous thin films: properties and applications. *Chem. Soc. Rev.* **2013**, *42*, 4198−4216.

(2) Laurenti, M.; Grochowicz, M.; Cauda, V. Porous ZnO/2−Hydroxyethyl Methacrylate Eluting Coatings for Ureteral Stent Applications. *Coatings* **2018**, *8*, 376.

(3) Kumar, P.; Kim, K.-H.; Vellingiri, K.; Samaddar, P.; Kumar, P.; Deep, A.; Kumar, N. Hybrid porous thin films: Opportunities and challenges for sensing applications. *Biosens. Bioelectron.* **2018**, *104*, 120−137.

(4) Rapsomanikis, A.; Karageorgopoulos, D.; Lianos, P.; Stathatos, E. High performance perovskite solar cells with functional highly porous TiO_2 thin films constructed in ambient air. *Sol. Energy Mater. Sol. Cells* **2016**, *151*, 36−43.

(5) Park, J. Y.; Kim, H.-H.; Rana, D.; Jamwal, D.; Katoch, A. Surface-area-controlled synthesis of porous TiO_2 thin films for gas-sensing applications. *Nanotechnology* **2017**, *28*, No. 095502.

(6) Haffer, S.; Waitz, T.; Tiemann, M. Mesoporous In_2O_3 with Regular Morphology by Nanocasting: A Simple Relation between Defined Particle Shape and Growth Mechanism. *J. Phys. Chem. C* **2010**, *114*, 2075−2081.

(7) Liu, Z.; Jin, Z.; Li, W.; Qiu, J. Preparation of ZnO porous thin films by sol−gel method using PEG template. *Mater. Lett.* **2005**, *59*, 3620−3625.

(8) Liu, Z.; Jin, Z.; Li, W.; Qiu, J.; Zhao, J.; Liu, X. Synthesis of PS colloidal crystal templates and ordered ZnO porous thin films by dip-drawing method. *Appl. Surf. Sci.* **2006**, *252*, 5002−5009.

(9) Sarkar, K.; Rawolle, M.; Herzig, E. M.; Wang, W.; Buffet, A.; Roth, S. V.; Müller-Buschbaum, P. Custom-made morphologies of ZnO nanostructured films templated by a poly(styrene-block-ethylene oxide) diblock copolymer obtained by a sol-gel technique. *ChemSusChem* **2013**, *6*, 1414−1424.

(10) Tian, T.; Yin, S.; Tu, S.; Weindl, C. L.; Wienhold, K. S.; Liang, S.; Schwartzkopf, M.; Roth, S. V.; Müller-Buschbaum, P. Morphology Transformation Pathway of Block Copolymer-Directed Cooperative Self-Assembly of ZnO Hybrid Films Monitored In Situ during Slot-Die Coating. *Adv. Funct. Mater.* **2021**, *31*, No. 2105644.

(11) Shekhah, O.; Liu, J.; Fischer, R. A.; Wöll, C. MOF thin films: existing and future applications. *Chem. Soc. Rev.* **2011**, *40*, 1081−1106.

(12) van de Voorde, B.; Ameloot, R.; Stassen, I.; Everaert, M.; de Vos, D.; Tan, J. C. Mechanical properties of electrochemically synthesised metal−organic framework thin films. *J. Mater. Chem. C* **2013**, *1*, 7716−7724.

(13) Liu, J.; Wöll, C. Surface-supported metal-organic framework thin films: fabrication methods, applications, and challenges. *Chem. Soc. Rev.* **2017**, *46*, 5730−5770.

(14) Zhang, X.; Wan, K.; Subramanian, P.; Xu, M.; Luo, J.; Fransaer, J. Electrochemical deposition of metal−organic framework films and their applications. *J. Mater. Chem. A* **2020**, *8*, 7569−7587.

(15) Liu, G. Q.; Jin, Z. G.; Liu, X. X.; Wang, T.; Liu, Z. F. Anatase TiO_2 porous thin films prepared by sol-gel method using CTAB surfactant. *J. Sol-Gel Sci. Technol.* **2007**, *41*, 49−55.

(16) Lepoutre, S.; Smått, J.-H.; Laberty, C.; Amenitsch, H.; Grosso, D.; Lindén, M. Detailed study of the pore-filling processes during

nanocasting of mesoporous films using SnO_2/SiO_2 as a model system. *Microporous Mesoporous Mater.* **2009**, *123*, 185−192.
(17) Liu, Z.; Jin, Z.; Liu, X.; Fu, Y.; Liu, G. Fabrication of Ordered TiO_2 Porous Thin Films by Sol-Dipping PS Template Method. *J. Sol-Gel Sci. Technol.* **2006**, *38*, 73−78.
(18) Su, X.; Duan, G.; Xu, Z.; Zhou, F.; Cai, W. Structure and thickness-dependent gas sensing responses to NO_2 under UV irradiation for the multilayered ZnO micro/nanostructured porous thin films. *J. Colloid Interface Sci.* **2017**, *503*, 150−158.
(19) Bu, S. J.; Jin, Z. G.; Liu, X. X.; Yang, L. R.; Cheng, Z. J. Synthesis of TiO_2 porous thin films by polyethylene glycol templating and chemistry of the process. *J. Eur. Ceram. Soc.* **2005**, *25*, 673−679.
(20) Dai, P.; Zhang, G.; Chen, Y.; Jiang, H.; Feng, Z.; Lin, Z.; Zhan, J. Porous copper zinc tin sulfide thin film as photocathode for double junction photoelectrochemical solar cells. *Chem. Commun.* **2012**, *48*, 3006−3008.
(21) Ruan, H.; Li, Y.; Qiu, H.; Wei, M. Synthesis of porous NiS thin films on Ni foam substrate via an electrodeposition route and its application in lithium-ion batteries. *J. Alloys Compd.* **2014**, *588*, 357−360.
(22) Gosavi, S. R.; Nikam, C. P.; Shelke, A. R.; Patil, A. M.; Ryu, S.-W.; Bhat, J. S.; Deshpande, N. G. Chemical synthesis of porous web-structured CdS thin films for photosensor applications. *Mater. Chem. Phys.* **2015**, *160*, 244−250.
(23) Türker, Y.; Dag, Ö. Synthesis of mesostructured metal sulfide films using $[M(H_2O)_n](NO_3)_2$:P85 (M = Cd(ii) and Zn(ii)) liquid crystalline mesophases. *J. Mater. Chem.* **2008**, *18*, 3467−3473.
(24) Fischereder, A.; Martinez-Ricci, M. L.; Wolosiuk, A.; Haas, W.; Hofer, F.; Trimmel, G.; Soler-Illia, G. J. A. A. Mesoporous ZnS Thin Films Prepared by a Nanocasting Route. *Chem. Mater.* **2012**, *24*, 1837−1845.
(25) Türker, Y.; Karakaya, C.; Dag, Ö. Fabrication of mesoporous metal chalcogenide nanoflake silica thin films and spongy mesoporous CdS and CdSe. *Chemistry* **2012**, *18*, 3695−3705.
(26) Wang, Y.; Wu, Y.; Shirazi-Amin, A.; Kerns, P.; Fee, J.; He, J.; Jin, L.; Maric, R.; Suib, S. L. Direct Construction of Mesoporous Metal Sulfides via Reactive Spray Deposition Technology. *ACS Appl. Energy Mater.* **2019**, *2*, 2370−2374.
(27) Jen-La Plante, I.; Zeid, T. W.; Yang, P.; Mokari, T. Synthesis of metal sulfide nanomaterials via thermal decomposition of single-source precursors. *J. Mater. Chem.* **2010**, *20*, 6612−6617.
(28) Shen, S.; Zhang, Y.; Peng, L.; Xu, B.; Du, Y.; Deng, M.; Xu, H.; Wang, Q. Generalized synthesis of metal sulfide nanocrystals from single-source precursors: size, shape and chemical composition control and their properties. *CrystEngComm* **2011**, *13*, 4572−4579.
(29) Pradhan, N.; Katz, B.; Efrima, S. Synthesis of High-Quality Metal Sulfide Nanoparticles from Alkyl Xanthate Single Precursors in Alkylamine Solvents. *J. Phys. Chem. B* **2003**, *107*, 13843−13854.
(30) Vakalopoulou, E.; Buchmaier, C.; Pein, A.; Saf, R.; Fischer, R. C.; Torvisco, A.; Warchomicka, F.; Rath, T.; Trimmel, G. Synthesis and characterization of zinc di(O-2,2-dimethylpentan-3-yl dithiocarbonates) bearing pyridine or tetramethylethylenediamine coligands and investigation of their thermal conversion mechanisms towards nanocrystalline zinc sulfide. *Dalton Trans.* **2020**, *49*, 14564−14575.
(31) Buchmaier, C.; Rath, T.; Pirolt, F.; Knall, A.-C.; Kaschnitz, P.; Glatter, O.; Wewerka, K.; Hofer, F.; Kunert, B.; Krenn, K.; Trimmel, G. Room temperature synthesis of $CuInS_2$ nanocrystals. *RSC Adv.* **2016**, *6*, 106120−106129.
(32) Buchmaier, C.; Glänzer, M.; Torvisco, A.; Poelt, P.; Wewerka, K.; Kunert, B.; Gatterer, K.; Trimmel, G.; Rath, T. Nickel sulfide thin films and nanocrystals synthesized from nickel xanthate precursors. *J. Mater. Sci.* **2017**, *52*, 10898−10914.
(33) Rath, T.; Padeste, C.; Vockenhuber, M.; Fradler, C.; Edler, M.; Reichmann, A.; Letofsky-Papst, I.; Hofer, F.; Ekinci, Y.; Griesser, T. Direct extreme UV-lithographic conversion of metal xanthates into nanostructured metal sulfide layers for hybrid photovoltaics. *J. Mater. Chem. A* **2013**, *1*, 11135−11140.
(34) Alderhami, S. A.; Collison, D.; Lewis, D. J.; McNaughter, P. D.; O'Brien, P.; Spencer, B. F.; Vitorica-Yrezabal, I.; Whitehead, G. Accessing γ-Ga_2S_3 by solventless thermolysis of gallium xanthates: a low-temperature limit for crystalline products. *Dalton Trans.* **2019**, *48*, 15605−15612.
(35) McNaughter, P. D.; Saah, S. A.; Akhtar, M.; Abdulwahab, K.; Malik, M. A.; Raftery, J.; Awudza, J. A. M.; O'Brien, P. The effect of alkyl chain length on the structure of lead(II) xanthates and their decomposition to PbS in melt reactions. *Dalton Trans.* **2016**, *45*, 16345−16353.
(36) Rath, T.; MacLachlan, A. J.; Brown, M. D.; Haque, S. A. Structural, optical and charge generation properties of chalcostibite and tetrahedrite copper antimony sulfide thin films prepared from metal xanthates. *J. Mater. Chem. A* **2015**, *3*, 24155−24162.
(37) Bakly, A. A. K.; Spencer, B. F.; O'Brien, P. The deposition of thin films of cadmium zinc sulfide $Cd_{1-x}Zn_xS$ at 250 °C from spin-coated xanthato complexes: a potential route to window layers for photovoltaic cells. *J. Mater. Sci.* **2018**, *53*, 4360−4370.
(38) Buckingham, M. A.; Catherall, A. L.; Hill, M. S.; Johnson, A. L.; Parish, J. D. Aerosol-Assisted Chemical Vapor Deposition of CdS from Xanthate Single Source Precursors. *Cryst. Growth Des.* **2017**, *17*, 907−912.
(39) Tamilselvan, M.; Byregowda, A.; Su, C.-Y.; Tseng, C.-J.; Bhattacharyya, A. J. Planar Heterojunction Solar Cell Employing a Single-Source Precursor Solution-Processed Sb_2S_3 Thin Film as the Light Absorber. *ACS Omega* **2019**, *4*, 11380−11387.
(40) Al-Shakban, M.; Xie, Z.; Savjani, N.; Malik, M. A.; O'Brien, P. A facile method for the production of SnS thin films from melt reactions. *J. Mater. Sci.* **2016**, *51*, 6166−6172.
(41) Al-Shakban, M.; Matthews, P. D.; Savjani, N.; Zhong, X. L.; Wang, Y.; Missous, M.; O'Brien, P. The synthesis and characterization of Cu_2ZnSnS_4 thin films from melt reactions using xanthate precursors. *J. Mater. Sci.* **2017**, *52*, 12761−12771.
(42) Dunst, S.; Rath, T.; Reichmann, A.; Chien, H.-T.; Friedel, B.; Trimmel, G. A comparison of copper indium sulfide-polymer nanocomposite solar cells in inverted and regular device architecture. *Synth. Met.* **2016**, *222*, 115−123.
(43) Barreca, D.; Tondello, E.; Lydon, D.; Spalding, T. R.; Fabrizio, M. Single-Source CVD of Zinc Sulfide-Based Thin Films from Zinc bis(y-Ethylxanthate). *Chem. Vap. Deposition* **2003**, *9*, 93−98.
(44) Al-Shakban, M.; Matthews, P. D.; Lewis, E. A.; Raftery, J.; Vitorica-Yrezabal, I.; Haigh, S. J.; Lewis, D. J.; O'Brien, P. Chemical vapor deposition of tin sulfide from diorganotin(IV) dixanthates. *J. Mater. Sci.* **2019**, *54*, 2315−2323.
(45) Barreca, D.; Gasparotto, A.; Maragno, C.; Seraglia, R.; Tondello, E.; Venzo, A.; Krishnan, V.; Bertagnolli, H. Synthesis and characterization of zinc bis(*O*-isopropylxanthate) as a single-source chemical vapor deposition precursor for ZnS. *Appl. Organometal. Chem.* **2005**, *19*, 1002−1009.
(46) Rath, T.; Edler, M.; Haas, W.; Fischereder, A.; Moscher, S.; Schenk, A.; Trattnig, R.; Sezen, M.; Mauthner, G.; Pein, A.; Meischler, D.; Bartl, K.; Saf, R.; Bansal, N.; Haque, S. A.; Hofer, F.; List, E. J.; Trimmel, G. A Direct Route Towards Polymer/Copper Indium Sulfide Nanocomposite Solar Cells. *Adv. Energy Mater.* **2011**, *1*, 1046−1050.
(47) Fischereder, A.; Schenk, A.; Rath, T.; Haas, W.; Delbos, S.; Gougaud, C.; Naghavi, N.; Pateter, A.; Saf, R.; Schenk, D.; Edler, M.; Bohnemann, K.; Reichmann, A.; Chernev, B.; Hofer, F.; Trimmel, G. Solution-processed copper zinc tin sulfide thin films from metal xanthate precursors. *Monatsh. Chem.* **2013**, *144*, 273−283.
(48) Vagvala, T. C.; Pandey, S. S.; Krishnamurthy, S.; Hayase, S. Effect of Varying Alkyl Chain Length on Thermal Decomposition Temperature of Zinc(II) Xanthates and its Impact on Curing of Epoxy Resin. *Z. Anorg. Allg. Chem.* **2016**, *642*, 134−139.
(49) Shombe, G. B.; Khan, M. D.; Zequine, C.; Zhao, C.; Gupta, R. K.; Revaprasadu, N. Direct solvent free synthesis of bare α-NiS, β-NiS and α-β-NiS composite as excellent electrocatalysts: Effect of self-capping on supercapacitance and overall water splitting activity. *Sci. Rep.* **2020**, *10*, 3260.
(50) Akram, R.; Khan, M. D.; Zequine, C.; Zhao, C.; Gupta, R. K.; Akhtar, M.; Akhtar, J.; Malik, M. A.; Revaprasadu, N.; Bhatti, M. H.

https://doi.org/10.1021/acsanm.1c04206
ACS Appl. Nano Mater. 2022, 5, 1508−1520

Cobalt sulfide nanoparticles: Synthesis, water splitting and supercapacitance studies. *Mater. Sci. Semicond. Process.* **2020**, *109*, No. 104925.
(51) Hao, H.; Lang, X. Metal Sulfide Photocatalysis: Visible-Light-Induced Organic Transformations. *ChemCatChem* **2019**, *11*, 1378−1393.
(52) Chandrasekaran, S.; Yao, L.; Deng, L.; Bowen, C.; Zhang, Y.; Chen, S.; Lin, Z.; Peng, F.; Zhang, P. Recent advances in metal sulfides: from controlled fabrication to electrocatalytic, photocatalytic and photoelectrochemical water splitting and beyond. *Chem. Soc. Rev.* **2019**, *48*, 4178−4280.
(53) Yu, X. Y.; David Lou, X. W. Mixed Metal Sulfides for Electrochemical Energy Storage and Conversion. *Adv. Energy Mater.* **2018**, *8*, No. 1701592.
(54) Ikeda, T.; Hagihara, H. The crystal structure of zinc ethylxanthate. *Acta Cryst.* **1966**, *21*, 919−927.
(55) Vagvala, T. C.; Kapil, G.; Pandey, S. S.; Ogomi, Y.; Hayase, S. Nonisothermal curing kinetics of epoxy resin composite utilizing Ga(III) xanthate as a latent catalyst. *J. Appl. Polym. Sci.* **2015**, *132*, 42149.
(56) MacLachlan, A. J.; Rath, T.; Cappel, U. B.; Dowland, S. A.; Amenitsch, H.; Knall, A.-C.; Buchmaier, C.; Trimmel, G.; Nelson, J.; Haque, S. A. Polymer/Nanocrystal Hybrid Solar Cells: Influence of Molecular Precursor Design on Film Nanomorphology, Charge Generation and Device Performance. *Adv. Funct. Mater.* **2015**, *25*, 409−420.
(57) Jiang, X.; Zhang, W.; Zhong, Y.; Wang, S. Synthesis and Structure of the Cadmium (II) Complex: $[Cd(C_5H_5N)_2(S_2CO\text{-}n\text{-}C_4H_9)_2]$. *Molecules* **2002**, *7*, 549−553.
(58) Raston, C. L.; White, A. H.; Winter, G. Crystal Structure and Electronic Spectrum for Bis(0-ethylxanthato)pyridinezinc(II). *Aust. J. Chem.* **1976**, *29*, 731−738.
(59) Fuertes, M. C.; Marchena, M.; Marchi, M. C.; Wolosiuk, A.; Soler-Illia, G. J. A. A. Controlled deposition of silver nanoparticles in mesoporous single- or multilayer thin films: from tuned pore filling to selective spatial location of nanometric objects. *Small* **2009**, *5*, 272−280.
(60) Bourgeois, A.; Turcant, Y.; Walsh, C.; Defranoux, C. Ellipsometry porosimetry (EP): thin film porosimetry by coupling an adsorption setting with an optical measurement, highlights on additional adsorption results. *Adsorption* **2008**, *14*, 457−465.
(61) Factorovich, M. H.; Molinero, V.; Scherlis, D. A. Vapor pressure of water nanodroplets. *J. Am. Chem. Soc.* **2014**, *136*, 4508−4514.
(62) Kim, S.; Kim, D.; Kim, J.; An, S.; Jhe, W. Direct Evidence for Curvature-Dependent Surface Tension in Capillary Condensation: Kelvin Equation at Molecular Scale. *Phys. Rev. X* **2018**, *8*, 041046.
(63) Glatter, O.; Kratky, O. Small Angle X-Ray Scattering. *Chapter 2 General Theory by Porod*; Academic Press INC LTD., 1982.
(64) Ehmann, H. M. A.; Werzer, O.; Pachmajer, S.; Mohan, T.; Amenitsch, H.; Resel, R.; Kornherr, A.; Stana-Kleinschek, K.; Kontturi, E.; Spirk, S. Surface-Sensitive Approach to Interpreting Supramolecular Rearrangements in Cellulose by Synchrotron Grazing Incidence Small-Angle X-ray Scattering. *ACS Macro Lett.* **2015**, *4*, 713−716.
(65) Mehra, R.; Pancholi, M. Acoustic, Thermodynamic, Viscometric and Volumetric Studies in Multicomponent System of Hexane + 1-Dodecanol + Cyclohexane with Respect to Temperature. *Z. Phys. Chem.* **2007**, *221*, 847−866.
(66) Lide, D. R., Ed. *CRC Handbook of Chemistry and Physics*, 84th Edition, 2003-2004.
(67) Florio, G. M.; Werblowsky, T. L.; Ilan, B.; Müller, T.; Berne, B. J.; Flynn, G. W. Chain-Length Effects on the Self-Assembly of Short 1-Bromoalkane and n -Alkane Monolayers on Graphite. *J. Phys. Chem. C* **2008**, *112*, 18067−18075.
(68) Hashimoto, Y.; Sato, T.; Goto, R.; Nagao, Y.; Mitsuishi, M.; Nagano, S.; Matsui, J. In-plane oriented highly ordered lamellar structure formation of poly(N-dodecylacrylamide) induced by humid annealing. *RSC Adv.* **2017**, *7*, 6631−6635.
(69) Rauscher, M.; Salditt, T.; Spohn, H. Small-angle x-ray scattering under grazing incidence: The cross section in the distorted-wave Born approximation. *Phys. Rev. B* **1995**, *52*, 16855−16863.
(70) Tolan, M. X-Ray Scattering from Soft-Matter Thin Films: Materials Science and Basic Research; *Springer Tracts in Modern Physics*, *148*; Springer-Verlag: Berlin Heidelberg, 1999.
(71) Campbell, E. D. On the Preparation of Potassium Xanthate for Nickel Determinations. *J. Am. Chem. Soc.* **1900**, *22*, 307−308.
(72) González-Roura, A.; Casas, J.; Llebaria, A. Synthesis and phospholipase C inhibitory activity of D609 diastereomers. *Lipids* **2002**, *37*, 401−406.
(73) Gottlieb, H. E.; Kotlyar, V.; Nudelman, A. NMR Chemical Shifts of Common Laboratory Solvents as Trace Impurities. *J. Org. Chem.* **1997**, *62*, 7512−7515.
(74) *Bruker APEX2 and SAINT*. Bruker AXS Inc.: Madison, Wisconsin, USA, 2012.
(75) Sheldrick, G. M. *CELL_NOW*; Univ. Göttingen, Ger, 2008.
(76) Blessing, R. H. An empirical correction for absorption anisotropy. *Acta Crystallogr. A* **1995**, *51*, 33−38.
(77) Sheldrick, G. M., *SADABS, Version 2.10, Siemens Area Detector Correction*; Universität Göttingen, Germany, 2003.
(78) Sheldrick, G. M. SHELXT - integrated space-group and crystal-structure determination. *Acta Crystallogr. A* **2015**, *71*, 3−8.
(79) Sheldrick, G. M. Phase annealing in SHELX-90: direct methods for larger structures. *Acta Crystallogr. A* **1990**, *46*, 467−473.
(80) Sheldrick, G. M. A short history of SHELX. *Acta Crystallogr. A* **2008**, *64*, 112−122.
(81) Sheldrick, G. M. Crystal structure refinement with SHELXL. *Acta Crystallogr. C* **2015**, *71*, 3−8.
(82) Sheldrick, G. M. *SHELXS97*; Univ. Göttingen, Ger, 1997.
(83) Hübschle, C. B.; Sheldrick, G. M.; Dittrich, B. ShelXle: a Qt graphical user interface for SHELXL. *J. Appl. Crystallogr.* **2011**, *44*, 1281−1284.
(84) Spek, A. L. Single-crystal structure validation with the program PLATON. *J. Appl. Crystallogr.* **2003**, *36*, 7−13.
(85) Spek, A. L. Structure validation in chemical crystallography. *Acta Crystallogr. D* **2009**, *65*, 148−155.
(86) Putz, H.; Brandenburg, K. *Diamond - Crystal and Molecular Structure Visualization, 3.2i, Crystal Impact*.
(87) Westrip, S. P. publCIF : software for editing, validating and formatting crystallographic information files. *J. Appl. Crystallogr.* **2010**, *43*, 920−925.
(88) Dolomanov, O. V.; Bourhis, L. J.; Gildea, R. J.; Howard, J. A. K.; Puschmann, H. OLEX2: a complete structure solution, refinement and analysis program. *J. Appl. Crystallogr.* **2009**, *42*, 339−341.
(89) Amenitsch, H.; Rappolt, M.; Kriechbaum, M.; Mio, H.; Laggner, P.; Bernstorff, S. First performance assessment of the small-angle X-ray scattering beamline at ELETTRA. *J. Synchrotron Radiat.* **1998**, *5*, 506−508.
(90) Burian, M.; Meisenbichler, C.; Naumenko, D.; Amenitsch, H. SAXSDOG: open software for real-time azimuthal integration of 2D scattering images. http://arxiv.org/pdf/2007.02022v1.

https://doi.org/10.1021/acsanm.1c04206
ACS Appl. Nano Mater. 2022, 5, 1508−1520